Theoretical and Applied Fracture Mechanics 110 (2020) 102827

Contents lists available at ScienceDirect

Theoretical and Applied Fracture Mechanics

journal homepage: www.elsevier.com/locate/tafmec

# Evaluating stress intensity factors for surface cracks in an orthotropic steel deck accounting for the welding residual stresses

Bin Qiang [a,b], Xin Wang [b,*]

[a] Department of Bridge Engineering, Southwest Jiaotong University, Chengdu, Sichuan 610031, China
[b] Department of Mechanical and Aerospace Engineering, Carleton University, Ottawa, Ontario K1S 5B6, Canada

ARTICLE INFO

*Keywords:*
Orthotropic steel deck
Welding residual stress
Stress intensity factor
Surface crack
Weight function method

ABSTRACT

The welding residual stresses (WRSs) in an orthotropic steel deck were investigated via experimental measurement and finite-element simulation. Both the surface and through-thickness WRSs were obtained. The simulated residual stress fields were in reasonable agreement with the measured results. The weight function method (WFM) was then adopted to investigate the effects of WRSs on stress intensity factors (SIFs) of semi-elliptical surface crack. The surface crack was subjected to a combination of far-field load and through-thickness WRSs, and different crack aspect ratios and relative depths were analyzed. The results reveal that the transverse residual stresses have prominent effects on SIFs: for the surface point, which is always located in the tensile stress region, its SIFs increase substantially with crack growing ($a/t$ increasing); for the deepest point, WRSs lead to some SIFs increase with lower growth rate and some SIFs decrease continuously. This is due to that, as $a/t$ increasing, the WRS level at crack tip location gradually decreases from the high tensile stress region, even into the compressive stress region.

## 1. Introduction

Orthotropic steel decks (OSD), stiffened by a series of longitudinal ribs and transverse cross beams, have a good overall performance due to rapid erection, easy assembly, and good load-carrying capacity in proportion to their weight. With these advantages, OSD has been widely used in many engineering structures, such as long-span bridges. However, one prominent disadvantage is that the rib-to-deck welded joint usually experiences fatigue cracking problems, due to the stress concentration of the structural detail stress, welding defect and welding residual stress (WRS) around the joint. This problem has seriously affected the structural safety and the application of OSD.

Welding has emerged as a widely used method for joining OSD structures. Meanwhile, WRS due to welding process is inevitably induced in the weld joints [1,2]. Several researchers have conducted a series of residual stress measurements for OSD to understand the WRS distribution. Kitada et al. [3] measured the WRS of three U-rib stiffened plates with different thickness and different steels via the sectioning method. Zhao et al. [4] used the hole-drilling method to carry out WRS measurement of hybrid steel U-rib stiffened plates with different size parameters and materials. Puymbroeck et al. [5] determined the RS distribution for the deck plate and longitudinal stiffener of the OSD by incremental hole-drilling method. These measurements only focused on the surface welding residual stresses, however, previous works [6–8] showed that through thickness of welding residual stresses have obvious spatial distribution properties. Gadallah et al. [9] performed the measurement of residual stress distributions at the weld root of rib-to-deck joints using the contour method; the result also revealed that through-thickness distribution of WRS has a large stress gradient. Residual stress significantly affects fatigue crack growth rates, with compressive residual stress slowing crack growth and tensile residual stress accelerating it [10].

Methodology based on fracture mechanics was commonly used to predict fatigue crack growth behavior of U rib-to-deck welded joint. Xiao et al. [11] investigated the transverse stresses and determined the design fatigue strength based on the crack propagation analysis. The analyses show that the surface stresses in the deck plate are much larger than those in the rib wall in the case of 75% weld penetration into the rib wall, and increasing the distribution area of wheel load or the thickness of deck plate can reduce the stress range of the deck plate and increase the fatigue life of the joint. Nguyen et al. [12] predicted the fatigue strength using fracture mechanics analysis for an orthotropic steel deck under light-weight vehicle loading. Three-level models were used to

* Corresponding author.
*E-mail address:* xin.wang@carleton.ca (X. Wang).

https://doi.org/10.1016/j.tafmec.2020.102827
Received 13 August 2020; Received in revised form 3 November 2020; Accepted 4 November 2020
Available online 10 November 2020

**Nomenclature**

| | |
|---|---|
| $a$ | crack length for semi-elliptical surface crack |
| $a_f$, $a_r$ | length of the front and rear ellipsoidal quadrants |
| $A$ | deepest point of surface crack |
| $A_0$, $A_1$, $A_2$, $A_3$ | parameters of least squares fitting for $Y_1$ |
| $b$ | half width of the double-ellipsoidal heat source model |
| $B$ | surface point of surface crack |
| $B_0$, $B_1$, $B_2$, $B_3$ | parameters of least squares fitting for $Y_0$ |
| $c$ | half width of a semi-elliptical crack |
| $c_h$ | half height for the double-ellipsoidal heat source model |
| $C_0$, $C_1$, $C_2$ | parameters of least squares fitting for $F_0$ |
| $d$ | distance from the weld toe line |
| $D_0$, $D_1$, $D_2$ | parameters of least squares fitting for $F_1$ |
| $\varepsilon_0$ | emissivity |
| $E$ | Young's modulus |
| $f_f$, $f_r$ | heat input fraction for the front and rear ellipsoidal quadrants |
| $F$ | boundary correction factor |
| $F_0$, $F_1$ | boundary correction factors for the reference stress intensity factors $K^B_{1r}$ and $K^B_{2r}$ |
| $J$ | $J$-integral |
| $h_c$ | heat transfer coefficient |
| $I$ | current |
| $K$ | stress intensity factor |
| $K^A_{1r}$, $K^A_{2r}$ | reference stress intensity factors of deepest point in a semi-elliptic surface crack |
| $K^B_{1r}$, $K^B_{2r}$ | reference stress intensity factors of surface point in a semi-elliptic surface crack |
| $M_{1A}$, $M_{2A}$, $M_{3A}$ | weight function parameters for deepest point of a surface crack |
| $M_{1B}$, $M_{2B}$, $M_{3B}$ | weight function parameters for surface point of a surface crack |
| $M_{A0}$, $M_{A1}$, $M_{B0}$, $M_{B1}$ | parameters to account for the effect of attachment with different weld angles |
| $m(z, a)$, $m_A(z, a)$, $m_B(z, a)$ | weight functions |
| $q_f(x, y, z)$, $q_r(x, y, z)$ | heat flux for front and rear ellipsoidal heat source model |
| $q_c$ | thermal convection |
| $q_r$ | thermal radiation |
| $Q$ | shape factor for an ellipse |
| $Q_h$ | total energy input for double-ellipsoidal heat source model |
| $t$ | plate thickness |
| $U$ | voltage |
| $Y_0$, $Y_1$ | boundary correction factors for the reference stress intensity factors $K^A_{1r}$ and $K^A_{2r}$ |
| $s_0$ | Stefan–Boltzmann constant |
| $\sigma_0$ | characteristic stress or nominal stress or external load |
| $\sigma_x$ | longitudinal residual stress along the welding line |
| $\sigma_y$ | transverse residual stress perpendicular to the weld line |
| $\sigma_{y01}$, $\sigma_{y02}$ | effective stresses for different combinations of external stress and welding residual stresses along the different pathes |
| $T_0$ | ambient temperature |
| $T_s$ | surface temperature of the weldment |
| $\phi$ | weld angles (degree) |
| $\sigma_{yield}$ | yield stress for the materials |
| $\sigma(z)$ | local stress distribution normal to the prospective crack plane |
| $\eta$ | heat energy transfer efficiency |
| $\nu$ | Poisson's ratio |
| LEFM | linear elastic fracture mechanics |
| OSD | orthotropic steel decks |
| SIF | stress intensity factor |
| WFM | weight function method |
| WRS | welding residual stress |

accurately evaluate the stress-intensity factors at the rib-to-diaphragm connection. The crack growth was simulated by numerical integration of the Paris' law with different sizes of initial cracks. Liu et al. [13] applied the structural hot spot stress approach to evaluate the rib–deck fatigue. The results show that the refined multi-sub-model considering the weld detail can reflect the mechanical behavior of the rib–deck joint. Yang et al. [14] investigated the fatigue strength of vertical stiffener welded joint in orthotropic steel decks, comparing the fatigue test results and the corresponding regression S-N curves. The results show that fatigue strength of partial penetration welded joint is slightly higher than full penetration welded joint before toe crack initiation. Both experimental measurement and numerical simulation play a significant role to understand and predict fatigue strength in orthotropic steel deck and have achieved many meaningful results. However, the welding residual stresses at the root have not yet been thoroughly quantified and their effects on stress intensity factors has not been considered in previous studies.

In the present study, an orthotropic steel deck with fully penetrated welded joint was manufactured and the welding process was simulated in the ABAQUS software [15]. The simulated welding residual stresses were compared with measured results by using the hole drilling method. Based on the obtained through-thickness distribution of transverse residual stress distribution at different paths, the weight function method (WFM) is used to investigate their effects on the stress intensity factors (SIFs) of semi-elliptical surface cracks with different crack sizes (aspect ratio and relative depth).

## 2. Measurement of welding residual stress

### 2.1. Specimen dimension and welding conditions

Geometry configurations, such as rib thickness, width, height, spacing, and deck thickness must be considered in OSD design. The test specimen composed of a single U-rib and flat plate was designed to have specific dimensions. As shown in the Fig. 1, the top deck with the dimension of 900 × 1000 × 14 mm$^3$; U rib thickness is 8 mm, rib height is 280 mm, rib spacing is 300 mm, and rib lower mouth width is 205 mm. The steel grade investigated in this experiment was Q345qD with a nominal yield strength $\sigma_{yield}$ = 345 MPa. Its nominal chemical

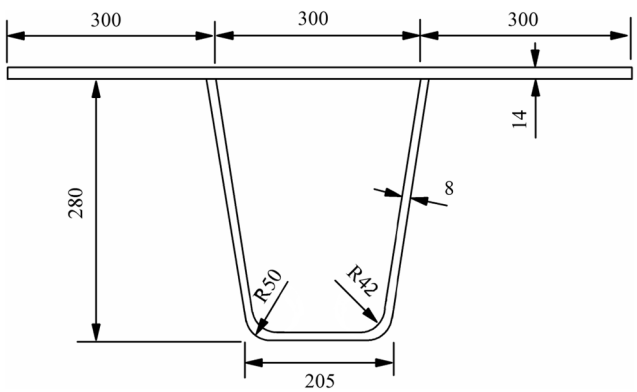


**Fig. 1.** Detail cross section of orthotropic steel deck (unit: mm).

composition and mechanical properties are listed in Table 1 [16]. The temperature-dependent material parameters of the thermo-physical properties (specific heat, thermal conductivity and density), mechanical properties (yield strength, Young's modulus, Poisson's ratio) and strain hardening property are summarized in Fig. 2; these were taken from literature data [17,18] and the SYSWELD material database [19]

The test specimen was made by a prominent steel bridge fabricator with the typical weld process. Before the welding, the test specimen was placed on the customized welding fixture, and both sides of the deck plate were fixed by the clamping device. And a natural groove (fit-up gap) of 12° was formed between the U rib and deck plate. And then, the tack welding was conducted to keep the pre-set gaps of the rib to deck along the entire length of the OSD. There was no preheating on the specimen. Full penetration is an obvious variable that may improve fatigue resistance. Because partial penetration welds inherently leave an unfused section of the rib at the root, which introduce a notch-like defect that could lead weld root failures. During the welding, a ceramic gasket was firstly installed at the inner joint of the U rib, and a submerged arc welding with double-supply multi-wire was used on the outside to form full penetration. This weld process is easy to achieve double-sided forming with single-sided welding. The weld pass-1 and pass-2 (see Fig. 3) were completed in turn. After the welding, the specimen cooled naturally to room temperature. The welding parameters of two weld passes are listed in Table 2.

### 2.2. Residual stress measurement

WRS measurement was performed on bottom surface of deck plate using hole-drilling method. The measurement path was perpendicular to the weld line, and the space between measurement points was 10 mm. The residual stress measurement was carried out on the middle section of the specimen as shown in Fig. 4. The measured surface stress was in a biaxial stress state, quantified by the longitudinal residual stress ($\sigma_x$) parallel to the weld direction and the transverse residual stress ($\sigma_y$) perpendicular to the weld direction. Residual stresses were calculated according ASTM E837-13a [20] taking into account the measured strains and strain release coefficients. The strain release coefficients calibrated under different stress levels ($0.3\sigma_{yield}$, $0.5\sigma_{yield}$, $0.7\sigma_{yield}$ and $0.9\sigma_{yield}$) [21] were adopted to eliminate the test error from the plastic deformation around the drilled hole, based on standard GB/T 31310-2014 [22].

## 3. Simulation of welding residual stress

### 3.1. Analysis of temperature field and stress field

The 3D finite-element model shown in Fig. 5 was developed in the ABAQUS. The model was the same size as the test specimen and its weld size was approximately equal to that of the weld cross-section of the specimen, as shown in Figs. 5 and 2. The number of weld passes and the welding sequence were simulated accordingly. The model had 83,400 elements and 91,341 nodes. To capture the stress gradient nearby the weld, the highly refined meshes were implemented around the weld region. Note to take advantage of the symmetric configuration of OSD, only half of the geometry was modeled.

First, the welding temperature field was computed by using the eight-node element DC3D8. The element "remove" and "add" technology was used to simulate the sequential deposition of weld filler. During the welding process, the volumetric heat source will move to the corresponding welded seam and elements will be added into weld groves step by step. As depicted in Fig. 6, the heat from the moving welding arc was simulated via a volumetric heat source with a double-ellipsoidal Goldak model [23]. And the DFLUX subroutine was adopted to load the heat source model along the different paths with moving speeds of 7.5 and 9.0 mm/s, respectively. The weld metal and base metal were assumed to have the same temperature-dependent physical and mechanical properties of Q345qD steel (see Fig. 2). The latent heat of fusion was set to 300 kJ /kg in the analysis between a liquid temperature of 1535 °C and a solid temperature of 1500 °C. The phase transformation in metal was neglected. For the thermal boundary conditions, heat loss due to convection ($q_c$) and radiation ($q_r$) were taken into account via Newton's law of cooling (Eq. (1)) and Stefan–Boltzman law (Eq. (2)), respectively [24].

$$q_c = -h_c(T_s - T_0) \tag{1}$$

$$q_r = -\varepsilon_0 s_0\left[(T + 273.15)^4 - (T_0 + 273.15)^4\right] \tag{2}$$

where $h_c$ is the heat transfer coefficient, is set to be 15 W/(m$^{2}$·°C); $T_s$ is the surface temperature of the weldment; and $T_0$ is the ambient temperature, is set to be 20 °C. $\varepsilon_0$ is the emissivity, and is assumed to be 0.85; and $s_0$ is the Stefan–Boltzmann constant.

The heat source is expressed in Eqs. (3) and (4):

$$q_f(x,y,z) = \frac{6\sqrt{3}f_f Q_h}{\pi a_f b c_h \sqrt{\pi}} \exp\left(-3\frac{x^2}{a_f^2}\right)\exp\left(-3\frac{y^2}{b^2}\right)\exp\left(-3\frac{z^2}{c_h^2}\right) \tag{3}$$

$$q_r(x,y,z) = \frac{6\sqrt{3}f_r Q_h}{\pi a_r b c_h \sqrt{\pi}} \exp\left(-3\frac{x^2}{a_r^2}\right)\exp\left(-3\frac{y^2}{b^2}\right)\exp\left(-3\frac{z^2}{c_h^2}\right) \tag{4}$$

where $q$ is the heat flux, $Q_h = \eta UI$ is the total energy input (for submerged arc welding, the heat energy transfer efficiency is $\eta = 0.9$), $a_f$, $a_r$, $b$, and $c_h$ are relative dimensions of Goldak's heat source, $x$, $y$, and $z$ denote the local coordinate system of the double ellipsoid model corresponding to the welded structure, and $f_f$ and $f_r$ are the heat input fraction in the front and rear ellipsoidal quadrants, respectively ($f_f = 1.2$, $f_r = 0.8$) [23].

For the temperature field simulation, accurate simulation of molten pool shape is a necessary base. Weld molten pool was defined as the portion whose temperature exceeds the melting temperature of 1500 °C for Q345qD. Through trial calculations for the double-ellipsoidal shape factors ($a_f$, $a_r$, $b$, and $c_h$), the weld-pool profile for each weld pass obtained in finite element simulation (see Fig. 7) was coincided with that observed on the weld cross-section of the experimental specimen. The shape parameters for the double-ellipsoidal heat source are summarized in Table 3.

After completing the simulation of temperature field, the temperature history of each node obtained from the heat transfer analysis, was imported as the initial state for the mechanical analysis. In this step, the temperature-dependent mechanical and strain hardening properties of Q345qD steel (see Fig. 2(b) and (c)) were used. A C3D8R hexahedral element was applied in the mechanical analysis. Except for different element types, the finite element model for both the thermal and stress analyses were the same. The boundary conditions for the finite element model were displacement constraints imposed at both ends of the deck, which was similar with that imposed on the specimen fabricated.

**Table 1**
Mechanical properties and chemical composition of Q345qD steel [16]

| Mechanical properties | Yield strength (MPa) | | Tensile strength (MPa) | | Elongation (%) |
|---|---|---|---|---|---|
| | 345 | | 490 | | 20 |
| Chemical composition (%) | C | Si | Mn | P | S |
| | 0.14 | 0.31 | 1.46 | 0.016 | 0.006 |

### 3.2. Residual stress results

#### 3.2.1. Surface residual stress

Fig. 8 shows the simulated surface WRSs distribution compared with those measured along the measured path of specimen bottom surface. In the figures, $d$ is the distance from the weld toe line. The uncertainties of

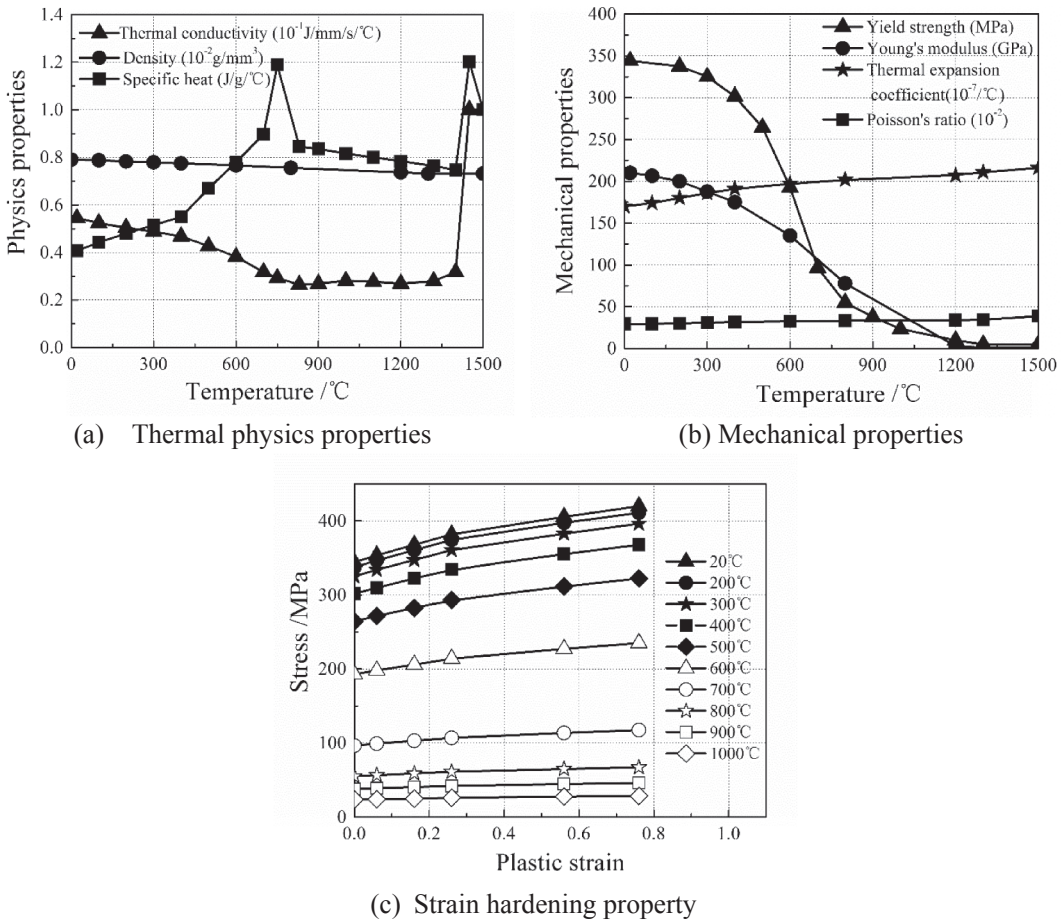


**Fig. 2.** Temperature-dependent material properties (a) thermo-physical, (b) mechanical and (c) strain hardening.

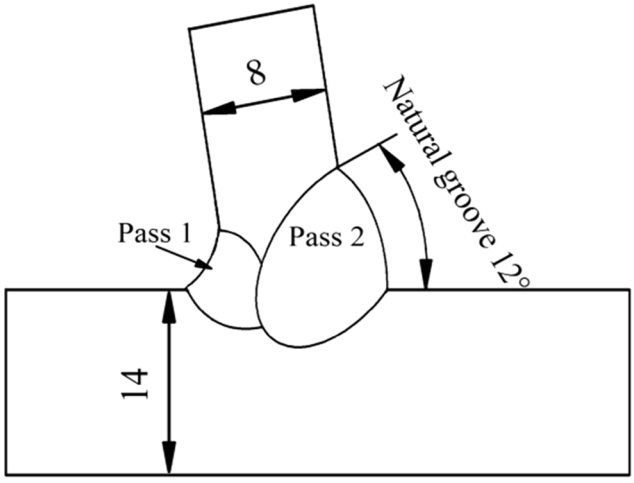


**Fig. 3.** Welding passes and condition (unit: mm).


**Fig. 4.** Schematic diagram showing measurement path.

**Table 2**
Welding parameters.

| Weld pass | Current (*I*)/A | *Voltage (U)/V* | Speed/ mm·min$^{-1}$ | Welding wire + flux |
|---|---|---|---|---|
| 1 | 410–440 | *30–33* | 430–460 | ER50-6(φ1.6) + TGF-SJ988U |
| 2 | 510–560 | *31–34* | 520–560 | H08MnA(φ3.2) + TGF-SJ988U |

the longitudinal and transverse stresses measured via hole-drilling method are determined to be ±39.8 and ±24.2 MPa, respectively. It can be seen that simulated curves agree reasonably with the measured data. The differences between the measured and simulated results may be attributed to errors introduced by the measurement process and by omitting from the numerical simulation the volumetric change caused by the solid-state phase transformation around the weld zone. Similar observations and related explanations were discussed by Francis et al. [25] and Rikken et al. [26].

As shown in Fig. 8(a), the simulated longitudinal peak stresses on the

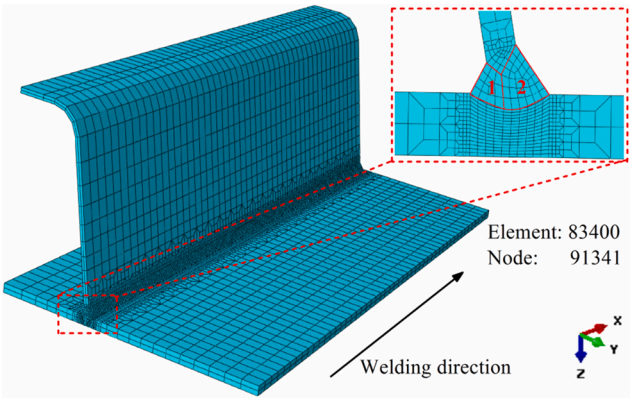


**Fig. 5.** Mesh details of the finite element model.

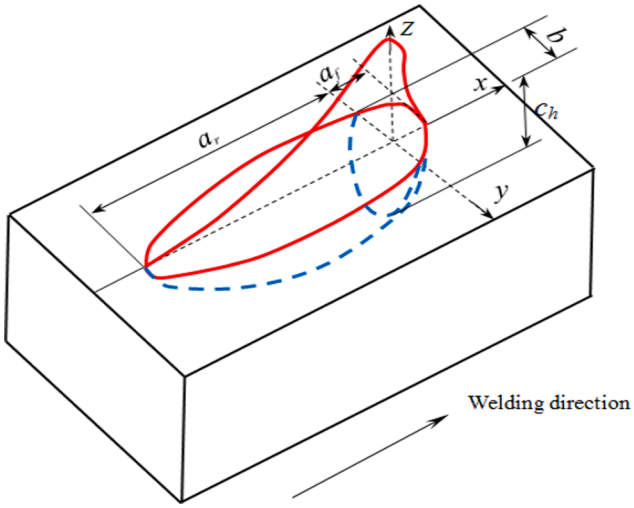


**Fig. 6.** Double-ellipsoidal heat-source model.

deck bottom surface are roughly 450 MPa, exceeding the initial yield strength of the material (345 MPa) and locating in the weld toe. As the distance from the weld toe increases, the longitudinal tensile stresses gradually decrease until they change into compressive stress. The distribution range of tensile stress is about 50 mm. The simulated transverse residual stresses in Fig. 8(b) are less than those in Fig. 8(a), whose peak stress at the bottom surface is about 100 MPa. Simulated transverse residual stresses generally are the tension stress with relative lower values.

### 3.2.2. *Internal residual stress*

Fig. 9 shows simulated stress contours of $\sigma_x$ and $\sigma_y$. Two sections are identified, section 1 (see Fig. 9) is the position of peak longitudinal stress which is the middle section, and peak transverse stress locates at surface of section 2 which is to the end about 70 mm. It can be seen from the Fig. 9 that both the $\sigma_x$ and $\sigma_y$ (S11 and S22 on Fig. 9) have high-value stress areas around the weld; through-thickness stresses vary along weld toe of different sections. A comparison of $\sigma_x$ and $\sigma_y$ shows that $\sigma_y$ has a lower stress gradient and stress level. The fixed constraint on the ends lead to $\sigma_y$ has a maximum stress on both ends of OSD. Transverse residual stress, $\sigma_y$, also has another peak located on the surface of section 2, which may be induced from the welding extinguishing arc. Fig. 10 shows the longitudinal and transverse stresses along the path1 and path 2 located in the weld toe of two different sections. These through-thickness residual stresses expressed in terms of depth normalized by plate thickness ($z/t$) and the residual stress normalized in the longitudinal or transverse direction ($\sigma_x/\sigma_{yield}$ or $\sigma_y/\sigma_{yield}$). Simulated longitudinal stress in Fig. 10 presents tensile stress with significant stress gradients. The peak stresses of $\sigma_x$ and $\sigma_y$ appear primarily at bottom deck surface affected by weld seam. As the position approaches the top surface of deck, the residual stresses gradually decrease, and $\sigma_y$ along the path 2 decreases to the compressive stress at the top surface. The longitudinal tensile peak stresses always exceed the material's yield stress $\sigma_{yield}$, while the transverse stress is lower than the longitudinal stress in the range of 0–0.5$\sigma_{yield}$.

## 4. Determination of stress intensity factors for surface cracks

It is already well-known that the weld detail of rib-to-deck joint is prone to reduced fatigue resistance. As shown in Fig. 11, fatigue cracking usually occurred at weld toe and then propagate through the deck plate. Thus, WRS at weld toe is necessary to take into account for

**Table 3**
Shape parameters of double-ellipsoidal heat source.

| Weld pass | $a_f$/mm | $a_r$/mm | $b$/mm | $c_h$/mm |
|---|---|---|---|---|
| 1 | 8.1 | 24.3 | 10.8 | 13.0 |
| 2 | 5.0 | 15.0 | 11.0 | 9.5 |

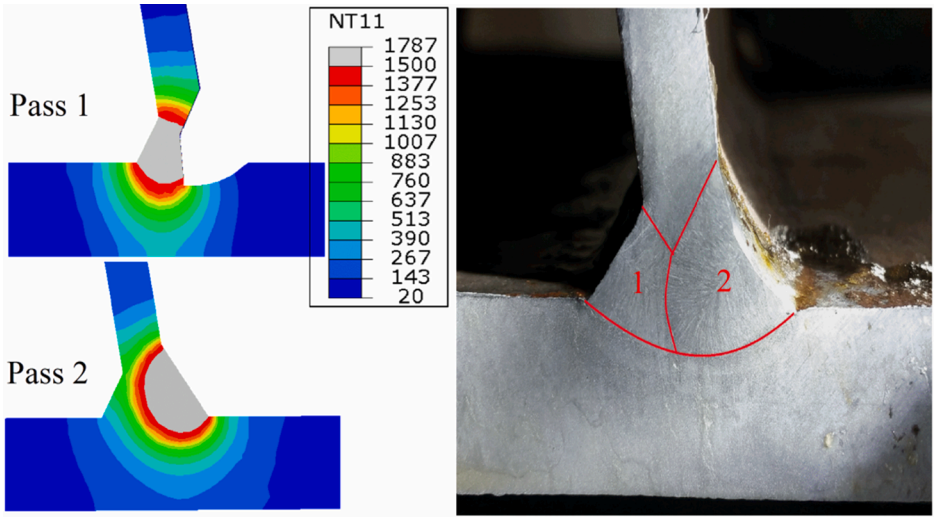


**Fig. 7.** Simulated weld-pool profiles and temperature contours for each weld pass.

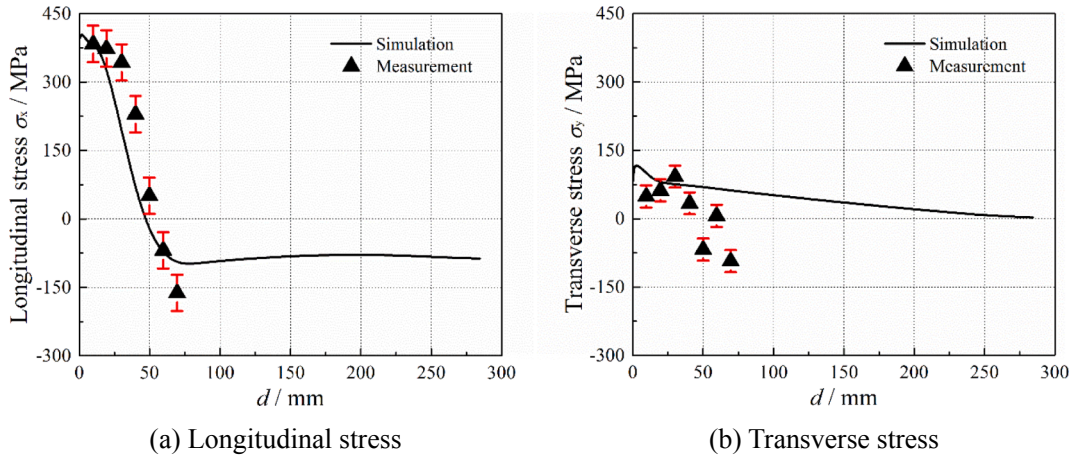


**Fig. 8.** Residual stress distributions on the deck bottom surface.

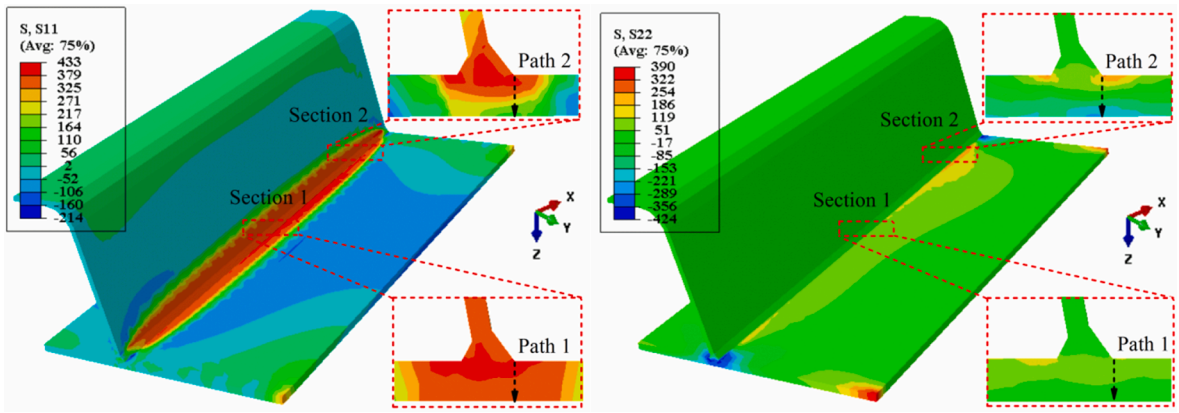


**Fig. 9.** Longitudinal and transverse residual stress contours.

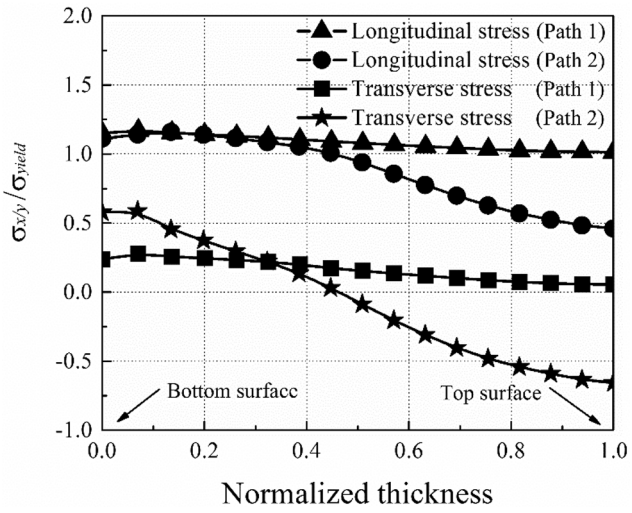


**Fig. 10.** Through-thickness residual stress variations at different paths along the weld toe.

the modification of the local fatigue stress. Based on the Paris' law, fatigue crack propagation rates are closely related to the SIFs. It has been shown that the WRS influences both the crack driving force and crack-tip constraint, which are key issues in application of fracture mechanics calculate the accurate SIFs values.

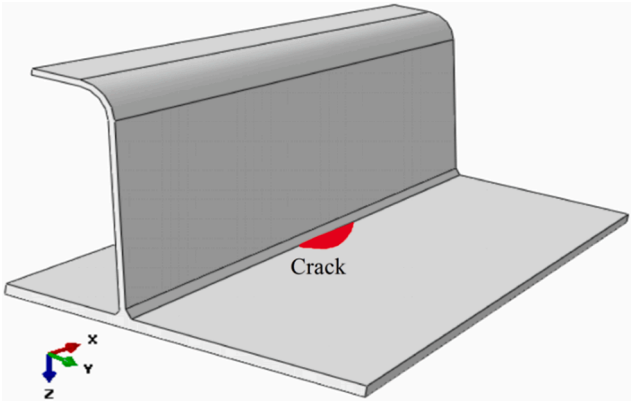


**Fig. 11.** A surface crack within the orthotropic steel deck (half of OSD shown).

Weight function method (WFM) and FEM are commonly used to calculate the SIFs of structure weld details. FEM, such as J-integral, and the peak stress method [27,28], can be used to quickly obtain the SIFs of complex geometries. Compared to FEM, WFM is more convenient to calculate the SIFs in the present OSD model.

### 4.1. Weight function method

The WFM is a very effective technique to determinate the SIF that are fundamental for fatigue crack growth analysis [29,30]. The weight

function is only related to crack geometry and has a remarkable computational efficiency. Thus, SIF can be easily obtained by integrating the product of any stress field and the appropriate weight function, which is particularly suited for the analysis of cracks in complex stress gradients. For semi-elliptical surface cracks, it was used to calculate SIF in plates [31,32] and in T-plate welded joints [33]. In a recent work, WFM was used for the study of the effect of residual stress on stress intensity factors for surface cracks in butt-welded steel plates [6].

For a surface cracks in OSD (Fig. 11), the geometrical configuration is very similar to surface cracks in T-plate welded joints. T-plate welded joint is one of the most common structural joints used in practical engineering. Wang and Lambert [33] derived the weight functions at the deepest and surface points of a semi-elliptical surface cracks in T-plate joint with a weld angle $\phi$ between 0 and 45°. As shown schematically in Fig. 12, $a$ is the crack length, $c$ is the half width of the crack, and $t$ is the plate thickness.

Mode-I stress intensity factors, $K$, can be calculated by integrating the weight function, $m(z, a)$, and the stress distribution, $\sigma(z)$, on the crack plane. The calculating expression is:

$$K = \int_0^a \sigma(z)\cdot m(z,a)dz \tag{5}$$

To calculate $K$, it was observed [31–33] that general weight functions $m(z, a)$ for the surface and deepest points of a semi-elliptical crack could be approximated using the following expression:

The weight function for the deepest point is

$$m_A(z,a) = \frac{2}{\sqrt{2\pi(a-z)}}\cdot\left[1 + M_{1A}\left(1-\frac{z}{a}\right)^{\frac{1}{2}} + M_{2A}\left(1-\frac{z}{a}\right) + M_{3A}\left(1-\frac{z}{a}\right)^{\frac{3}{2}}\right] \tag{6}$$

The weight function for the surface point is

$$m_B(z,a) = \frac{2}{\sqrt{\pi z}}\cdot\left[1 + M_{1B}\left(\frac{z}{a}\right)^{\frac{1}{2}} + M_{2B}\left(\frac{z}{a}\right) + M_{3B}\left(\frac{z}{a}\right)^{\frac{3}{2}}\right] \tag{7}$$

Here $M_{1A}$, $M_{2A}$, $M_{3A}$, $M_{1B}$, $M_{2B}$, and $M_{3B}$ are can be decided from two reference solutions and a third condition, as shown in following:

$$\begin{cases} M_{1A} = \dfrac{\pi}{\sqrt{2Q}}\left(4Y_0\cdot M_{A1} - 6Y_1\cdot M_{A0}\right) - \dfrac{24}{5} \\ M_{2A} = 3 \\ M_{3A} = 2\left(\dfrac{\pi}{\sqrt{2Q}}Y_0 - M_{1A} - 4\right) \end{cases} \tag{8}$$

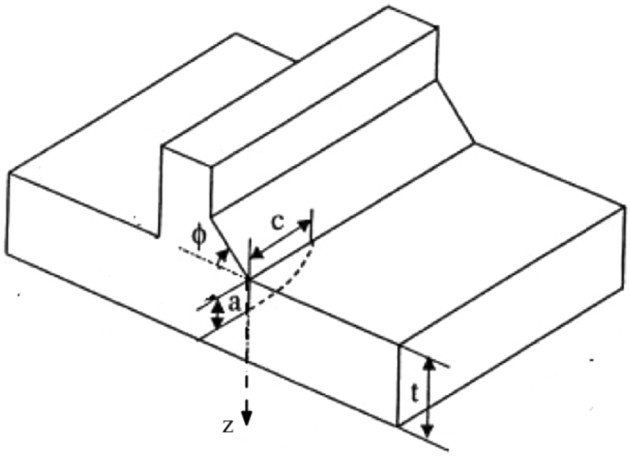


**Fig. 12.** Geometry and coordinate system for surface crack.

$$\begin{cases} M_{1B} = \dfrac{\pi}{\sqrt{4Q}}\left(30F_1\cdot M_{B1} - 18F_0\cdot M_{B0}\right) - 8 \\ M_{2B} = \dfrac{\pi}{\sqrt{4Q}}\left(60F_0\cdot M_{B0} - 90F_1\cdot M_{B1}\right) + 15 \\ M_{3B} = -(1 + M_{1B} + M_{2B}) \end{cases} \tag{9}$$

Detailed expressions for $M_{A0}$, $M_{A1}$, $Y_0$, $Y_1$, $M_{B0}$, $M_{B1}$, $F_0$ and $F_1$ derived for surface cracks in T-plate joints by Wang and Lambert [33] are presented in Appendix A.

The results from the WFM were normalized based on Eqs. (10) and (11):

$$F = \frac{K}{\sigma_0\sqrt{\pi a/Q}} \tag{10}$$

where $F$ is the boundary correction factor, $\sigma_0$ is the nominal stress, and $Q$ is the shape factor for an ellipse and is given by

$$Q = 1.0 + 1.464\left(\frac{a}{c}\right)^{1.65}, \quad \text{for } 0 \le a/c \le 1.0 \tag{11}$$

Next, we will use the weight function developed in [33] for T-plate joints to determine the stress intensity factors for surface cracks in OSD. Note the OSD weld angle is approximately 45°. Here, WFM was used to determine the mode-I SIFs for the assumed semi-elliptical surface cracks (see Fig. 11) with aspect ratio, $a/c$ = 0.05, 0.1, 0.2, 0.4, 0.6, 1.0 and relative depth, $a/t$ = 0.1, 0.2, 0.4, 0.6 with 45° weld angle. Recommended by the current design standard TB10091-2017 [34] the external load $\sigma_0$ was set to 71.9 MPa, which is the maximum allowable stress for rib-to-deck joint. When the external load $\sigma_0$ was applied to the far-field of rib-to-deck joint in y-direction, as shown in Fig. 11, the through-thickness distribution of transverse stress at the weld toe, for uncracked geometry, σ(z) is obtained and presented in Eq. (12). The simulated through-thickness transverse residual stress of path 1 and path 2 shown in Fig. 10, were used to calculate SIFs via WFM. Based on the superposition principle of LEFM, the effective stresses for different combinations of external stress and transverse residual stress are $\sigma_{y01} = \sigma_{y0} + \sigma_{path1}$ and $\sigma_{y02} = \sigma_{y0} + \sigma_{path2}$. Their specific distributions can be expressed in following Eqs. (13) and (14).

$$\sigma_{y0} = \sigma_0\left[0.7119 + 1.2114\left(\frac{z}{t}\right) - 2.9593\left(\frac{z}{t}\right)^2 + 3.5381\left(\frac{z}{t}\right)^3 - 1.4766\left(\frac{z}{t}\right)^4\right] \tag{12}$$

$$\sigma_{y01} = \sigma_0\left[1.8616 + 4.7127\left(\frac{z}{t}\right) - 30.922\left(\frac{z}{t}\right)^2 + 83.291\left(\frac{z}{t}\right)^3 - 122.96\left(\frac{z}{t}\right)^4 + 93.313\left(\frac{z}{t}\right)^5 - 28.009\left(\frac{z}{t}\right)^6\right] \tag{13}$$

$$\sigma_{y02} = \sigma_0\left[3.5343 + 1.9523\left(\frac{z}{t}\right) - 61.336\left(\frac{z}{t}\right)^2 + 227.11\left(\frac{z}{t}\right)^3 - 436.79\left(\frac{z}{t}\right)^4 + 399.12\left(\frac{z}{t}\right)^5 - 135.74\left(\frac{z}{t}\right)^6\right] \tag{14}$$

### 4.2. Finite element validation

First, we study the accuracy of the weight functions for T-plate from [33] for surface cracks in OSD. A 3D finite element model (as shown in Fig. 13) was built in ABAQUS to validate the SIFs from WFM. This model only has a specific geometric shape that crack aspect a/c = 0.6, depth ratio a/t = 0.6 and approximately 45° weld angle. Only half of the crack model was developed in ABAQUS, which having refined mesh around the crack front. To properly simulate the stress singularities in the analysis of surface cracks, in total 4886 elements were included in the mesh and the elements were the quadratic brick element with reduced

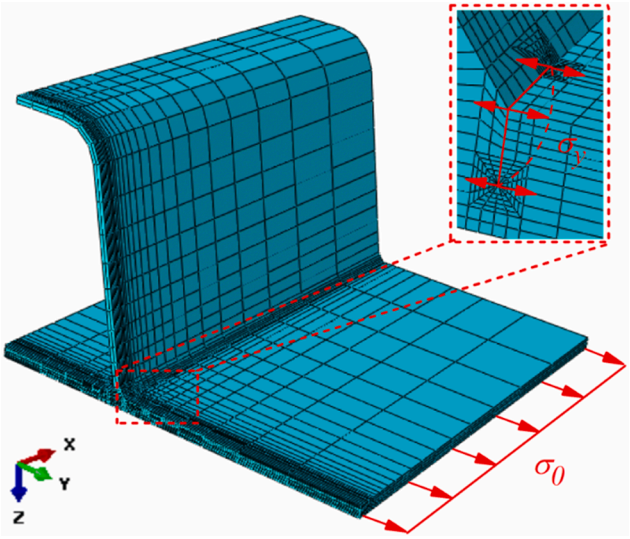


**Fig. 13.** Geometry and coordinate system for surface crack.

integration (C3D20R). The symmetry constraints of $y = 0$ and $x = 0$ were applied to the symmetry planes, respectively. One node of the model was also restrained the displacement of $z = 0$. The combination of transverse residual stresses and far-field constant stress were applied respectively to the crack surface and OSD end through the DLOAD subroutine. In ABAQUS, the SIFs were extracted using the J-integral technique calculated over a domain of the first five rings of elements surrounding the crack tip. A linear elastic material model was used in analysis with Young's modulus ($E$) of 207 GPa and Poisson's ratio ($\nu$) of 0.3. The SIFs can be obtained through the following relationship between $K$ and $J$ under plane strain and plane stress:

$$K = \begin{cases} \sqrt{\dfrac{JE}{(1-\nu^2)}} & \text{plane strain (deepest point)} \\ \sqrt{JE} & \text{plane stress (surface point)} \end{cases} \quad (15)$$

Table 4 summarizes the boundary correction factors $F$ for semi-elliptical surface cracks (a/c = 0.6, a/t = 0.6 with 45° weld angle) that were calculated via WFM and FEM under three different stress distributions. For surface and deepest points, all $F$ values of WFM agree reasonably well with those of FEM. The maximum relatively differences are within 14%. This can be concluded that the WFM of T-joint in [33] can be used to calculate the SIFs of U rib-to-deck joint and with acceptable accuracy.

### 4.3. Results for stress intensity factors

In the subsequent, WFM is used to calculate the SIFs of different geometry sizes ($a/c$ = 0.05, 0.1, 0.2, 0.4, 0.6, 1 and $a/t$ = 0.1, 0.2, 0.4, 0.6 with 45° weld angle) accounting for welding residual stresses.

**Table 4**
Boundary correction factors $F$ for semi-elliptical surface cracks (a/c = 0.6, a/t = 0.6 with 45° weld angle) under three different stress distributions.

| Position | Stress distribution | WFM | FEM | Difference $\frac{\lvert WFM - FEM \rvert}{FEM}$ |
|---|---|---|---|---|
| Surface | $\sigma_{y0}$ | 0.9918 | 1.0859 | 9% |
| | $\sigma_{y01}$ | 2.4358 | 2.2067 | 10% |
| | $\sigma_{y02}$ | 3.6451 | 3.2006 | 14% |
| Deepest | $\sigma_{y0}$ | 1.0524 | 1.0069 | 5% |
| | $\sigma_{y01}$ | 2.1695 | 1.9763 | 10% |
| | $\sigma_{y02}$ | 1.8158 | 1.5931 | 14% |

Figs. 14–16 show the SIFs for different surface-crack aspect ratios ($a/c$) and relative depths ($a/t$) obtained from the weight function method for different stress combinations, as shown in Eqs. (12)–(14).

Fig. 14 shows the SIF variation at $\sigma_{y0}$ distribution induced by a far-field constant tensile load. The results show the SIF ($F$) of the surface point increasing with aspect ratio ($a/c$), with the opposite variation for the deepest point. The values of $F$ for both the surface and deepest points increase nonlinearly with relative depth ($a/t$). The growth rate of $F$ is similar for the surface point with different $a/c$, while the growth rate of $F$ for deepest point noticeably increases as $a/c$ decreasing.

Figs. 15 and 16 show the SIFs of the surface crack subjected to the combination of $\sigma_{y0}$ and transverse residual stresses, at path1 and path2, respectively. A comparison of the results at the surface points in Figs. 14(a)–16(a) show that the WRSs along the path1 and path2 can significantly increase the SIF range. The SIFs of the surface point have similar evolution trends in Figs. 14(a)–16(a), excepting for the different amplitudes. It can easily be seen that, appearing at $a/c = 0.4$, 0.6 and 1, the SIFs of the surface point are almost coincident at $a/t = 0.6$.

At the deepest point, comparing to the SIFs results in Fig. 14(b), the SIFs show the different variation trends in Figs. 15(b) and 16(b). As shown in Fig. 15(b), for the $a/c = 0.6$ and 1, the SIFs increase firstly and then begin to decrease. This is because for path 1, the transverse residual stress is always tensile, with a small gradual stress reduction through the thickness (see Fig. 10). It is obviously shown in Fig. 16(b), for the $a/c$ = 0.2, 0.4, 0.6 and 1, the SIFs continued to decrease rapidly with the relative depth ($a/t$) increasing. This can be contributed to the tension–compression distribution of transverse stress along the path 2 which is different from that of path 1.

As mentioned above, the WRSs have significant effect on SIFs of surface crack. Tensile transverse residual stress will cause the SIF to increase. For the surface point, who is always located in the tensile stress region, its SIF increases substantially with crack growing ($a/t$ increasing). For the deepest point, WRS leads to some SIFs increase with lower growth rate and some SIFs decrease continuously. This is because that, as $a/t$ increasing, the stress level at the crack tip location gradually decreases from the tensile stress region, even into compressive stress region.

Clearly these observations indicate that welding residual stresses will have a marked effect on the fatigue crack propagation behavior of surface cracks in OSDs, and impact on their fatigue strength.

### 4.4. Discussion

It is important to note that WRSs are not always constant, and can relax during certain in-service conditions. Under high amplitude fatigue loading, for example, the initial residual stresses would relieve and redistribute by the early load cycles, and then tend to be stabilized. However, residual stress relaxation and redistribution is a complex nonlinear phenomenon which depends on the interaction of several factors such as the distribution state of residual stresses, the cyclic stress amplitude applied, the loading mode and direction, the number of cycles and the cyclic characteristics of the material, as discussed in [35–38]. In the present work, we have focused on the application of the WFM to investigate the effect of initial WRSs on the SIFs for semi-elliptical surface cracks; the possible effects of residual stress relaxation on SIFs were not considered. Based on the current SIFs results, further work can be carried out to develop proper models for fatigue crack propagation of surface cracks in OSDs that incorporate the effects of WRS relaxations and redistributions. It is our intention to study these effects in our future work.

## 5. Conclusions

In this paper, welding residual stresses were measured and simulated for an orthotropic steel deck. The WFM was validated by FEM, and then used to investigate the effects of WRSs on SIFs of semi-elliptical surface

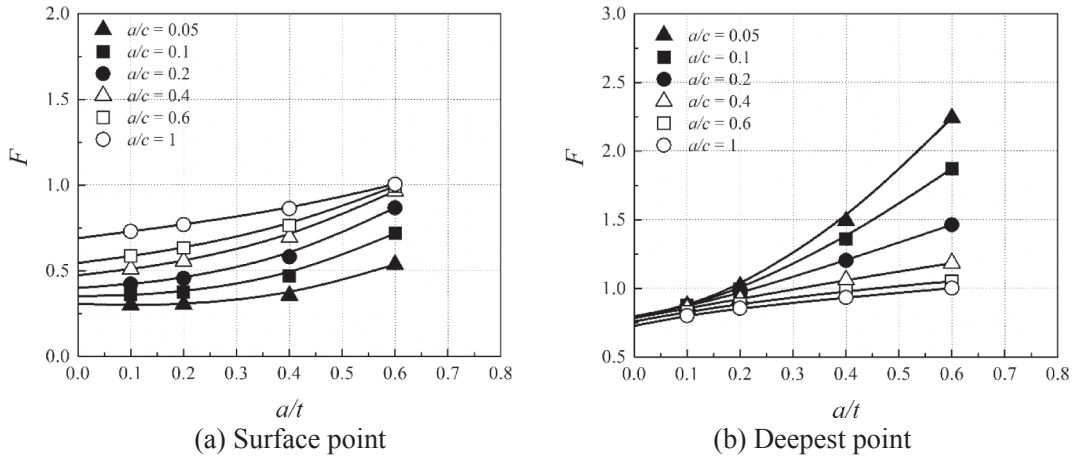


**Fig. 14.** SIF of surface crack subjected to external stress only.

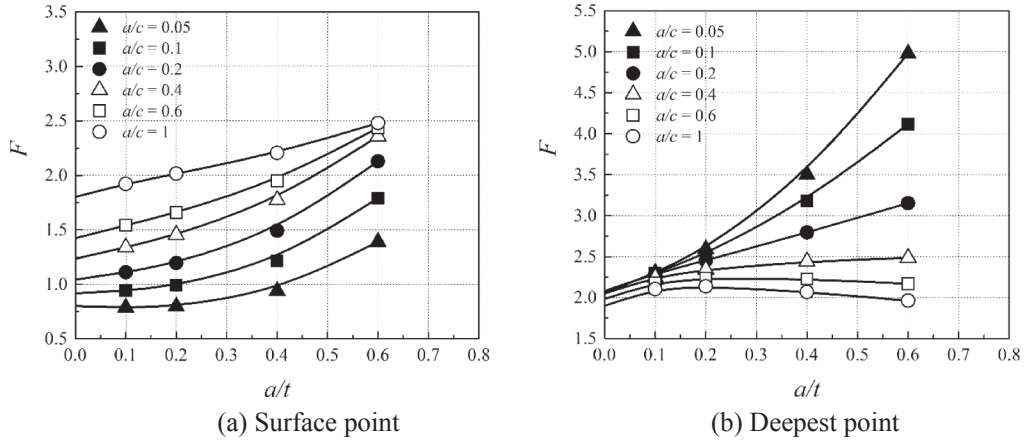


**Fig. 15.** SIF of surface crack subjected to both transverse residual stress along the path1 and external stress.

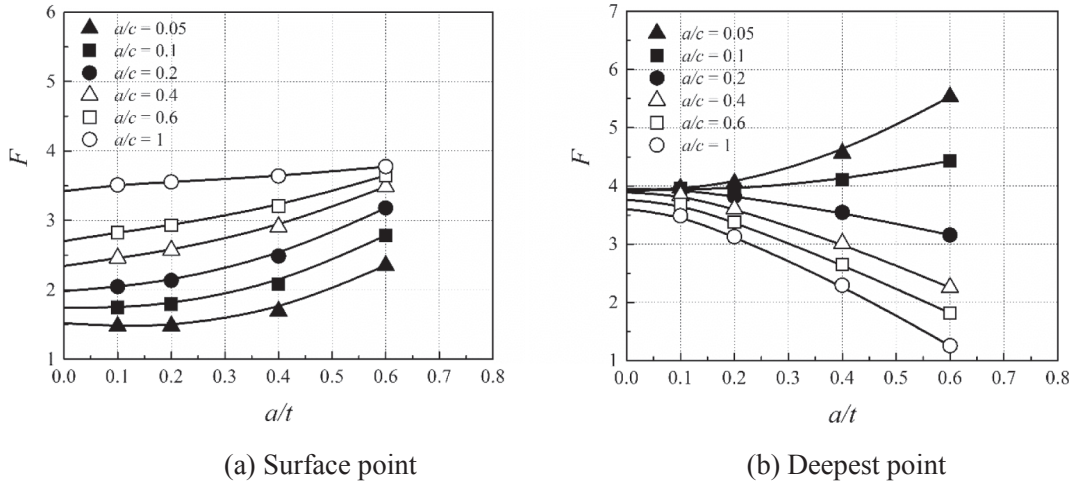


**Fig. 16.** SIF of surface crack subjected to both transverse residual stress along the path2 and external stress.

crack. Based on the results, the following conclusions can be drawn.

1. The simulated WRSs distributions are in reasonable agreement with the measured results. The peak surface stresses on deck bottom surface usually occur in fusion or heat affected zone. As the distance from the weld line center increases, the residual stresses decrease gradually until they change into compressive stress, with self-equilibrating tension–compression distributions.
2. The simulated through-thickness stresses $\sigma_x$ and $\sigma_y$ have their peak stresses located at weld toe of the deck bottom surface. As the position approaches the deck top surface, the residual stress gradually decreases, and $\sigma_y$ along the path 2 decreases to the compressive stress

at the top surface. The longitudinal tensile peak stresses always exceed the material's yield stress $\sigma_{yield}$, while the transverse stress is lower than the longitudinal stress in range of 0–0.5$\sigma_{yield}$.

3. For the semi-elliptical surface cracks (a/c = 0.6, a/t = 0.6 with 45° weld angle) loaded by three different stress distribution, the SIFs calculated via WFM and FEM are in good agreement. WFM can be used to calculate the SIFs of U rib-to-deck joint under combination of far-field stress and transverse residual stresses. For the surface point, which is always located in the tensile stress region, its SIFs increase substantially with crack growing ($a/t$ increasing). For the deepest point, WRS leads to certain SIFs increase with lower growth rate and certain SIFs decrease continuously. This is because that, as $a/t$ increasing, the stress level of crack tip location gradually decreases from the tensile stress region, even into compressive stress region.

## Declaration of Competing Interest

The authors declare that they have no known competing financial interests or personal relationships that could have appeared to influence the work reported in this paper.

## Acknowledgments

The authors gratefully acknowledge the financial support provided by the National Natural Science Foundation of China (Grant Nos. 51878562 and 51908473) and the Fundamental Research Funds for the Central Universities (Grant No. 2682020CX63). Financial support from Natural Science and Engineering Research Council of Canada (NSERC) is also gratefully acknowledged.

## Appendix A

In this appendix, the expressions used for the determination of weight functions $m_A(z, a)$ and $m_B(z, a)$ are summarized, they are from Ref. [33]. Expressions for reference stress intensity factors at the deepest point for a stress distribution constant through the thickness:

$$K_{1r}^{A} = \sigma_0\sqrt{\frac{\pi a}{Q}}Y_0\left(\frac{a}{c},\frac{a}{t}\right)\cdot M_{A0}\left(\varnothing,\frac{a}{c},\frac{a}{t}\right) \tag{A.1}$$

where

$$Y_0\left(\frac{a}{c},\frac{a}{t}\right) = B_0 + B_1\left(\frac{a}{t}\right)^2 + B_2\left(\frac{a}{t}\right)^4 + B_3\left(\frac{a}{t}\right)^6 \tag{A.2}$$

$$B_0 = 1.0929 + 0.2581\left(\frac{a}{c}\right) - 0.7703\left(\frac{a}{c}\right)^2 + 0.4394\left(\frac{a}{c}\right)^3 \tag{A.3}$$

$$B_1 = 0.456 - 3.045\left(\frac{a}{c}\right) + 2.007\left(\frac{a}{c}\right)^2 + \frac{1.0}{0.147 + \left(\frac{a}{c}\right)^{0.688}} \tag{A.4}$$

$$B_2 = 0.995 - \frac{1.0}{0.027 + \left(\frac{a}{c}\right)} + 22.0\left(1 - \frac{a}{c}\right)^{9.953} \tag{A.5}$$

$$B_3 = -1.459 + \frac{1.0}{0.014 + \left(\frac{a}{c}\right)} - 24.211\left(1.0 - \frac{a}{c}\right)^{8.071} \tag{A.6}$$

and

$$M_{A0}\left(\varnothing,\frac{a}{c},\frac{a}{t}\right) = \frac{(\varnothing-45)(\varnothing-30)}{1350} - \frac{\varnothing(\varnothing-45)}{450}M_{A0}^{\frac{\pi}{6}}\left(\frac{a}{c},\frac{a}{t}\right) + \frac{\varnothing(\varnothing-30)}{675}M_{A0}^{\frac{\pi}{4}}\left(\frac{a}{c},\frac{a}{t}\right) \tag{A.7}$$

$$\begin{aligned} M_{A0}^{\frac{\pi}{6}}\left(\frac{a}{c},\frac{a}{t}\right) = {} & 0.9037 + 0.2624\left(\frac{a}{t}\right) - 0.1294\left(\frac{a}{c}\right) + 0.1173\left(\frac{a}{t}\right)^2 + 0.4350\left(\frac{a}{c}\right)^2 - 0.4415\left(\frac{a}{t}\right)\left(\frac{a}{c}\right) - 0.3409\left(\frac{a}{t}\right)^3 - 0.2428\left(\frac{a}{c}\right)^3 + 0.02994\left(\frac{a}{t}\right)\left(\frac{a}{c}\right)^2 \\ & + 0.3122\left(\frac{a}{t}\right)^2\left(\frac{a}{c}\right) \end{aligned} \tag{A.8}$$

$$\begin{aligned} M_{A0}^{\frac{\pi}{4}}\left(\frac{a}{c},\frac{a}{t}\right) = {} & 0.8727 + 0.5252\left(\frac{a}{t}\right) - 0.2497\left(\frac{a}{c}\right) - 0.3144\left(\frac{a}{t}\right)^2 + 0.7695\left(\frac{a}{c}\right)^2 - 0.81028\left(\frac{a}{t}\right)\left(\frac{a}{c}\right) - 0.16645\left(\frac{a}{t}\right)^3 - 0.44419\left(\frac{a}{c}\right)^3 + 0.2454\left(\frac{a}{t}\right)\left(\frac{a}{c}\right)^2 \\ & + 0.5457\left(\frac{a}{t}\right)^2\left(\frac{a}{c}\right) \end{aligned} \tag{A.9}$$

Expressions for reference stress intensity factors at the deepest point for a stress distribution linearly decreasing through the thickness:

$$K_{2r}^{A} = \sigma_0\sqrt{\frac{\pi a}{Q}}Y_1\left(\frac{a}{c},\frac{a}{t}\right)M_{A1}\left(\varnothing,\frac{a}{c},\frac{a}{t}\right) \tag{A.10}$$

$$Y_1\left(\frac{a}{c},\frac{a}{t}\right) = A_0 + A_1\left(\frac{a}{t}\right)^2 + A_2\left(\frac{a}{t}\right)^4 + A_3\left(\frac{a}{t}\right)^6 \tag{A.11}$$

$$A_0 = 0.4537 + 0.1231\left(\frac{a}{c}\right) - 0.7412\left(\frac{a}{c}\right)^2 + 0.4600\left(\frac{a}{c}\right)^3 \tag{A.12}$$

$$A_1 = -1.652 + 1.665\left(\frac{a}{c}\right) - 0.534\left(\frac{a}{c}\right)^2 + \frac{1.0}{0.198 + \left(\frac{a}{c}\right)^{0.846}} \tag{A.13}$$

$$A_2 = 3.418 - 3.126\left(\frac{a}{c}\right) - \frac{1.0}{0.041 + \left(\frac{a}{c}\right)} + 17.259\left(1 - \frac{a}{c}\right)^{9.286} \tag{A.14}$$

$$A_3 = -4.228 + 3.643\left(\frac{a}{c}\right) + \frac{1.0}{0.020 + \left(\frac{a}{c}\right)} - 21.924\left(1.0 - \frac{a}{c}\right)^{9.203} \tag{A.15}$$

and

$$M_{A1}\left(\varnothing, \frac{a}{c}, \frac{a}{t}\right) = \frac{(\varnothing - 45)(\varnothing - 30)}{1350} - \frac{\varnothing(\varnothing - 45)}{450} M_{A1}^{\frac{\pi}{6}}\left(\frac{a}{c}, \frac{a}{t}\right) + \frac{\varnothing(\varnothing - 30)}{675} M_{A1}^{\frac{\pi}{4}}\left(\frac{a}{c}, \frac{a}{t}\right) \tag{A.16}$$

$$\begin{aligned} M_{A1}^{\frac{\pi}{6}}\left(\frac{a}{c}, \frac{a}{t}\right) = {} & 0.8310 + 0.4932\left(\frac{a}{t}\right) - 0.2219\left(\frac{a}{c}\right) + 0.4913\left(\frac{a}{t}\right)^2 + 0.9663\left(\frac{a}{c}\right)^2 - 0.9405\left(\frac{a}{t}\right)\left(\frac{a}{c}\right) - 1.2018\left(\frac{a}{t}\right)^3 - 0.5336\left(\frac{a}{c}\right)^3 + 0.02560\left(\frac{a}{t}\right)\left(\frac{a}{c}\right)^2 \\ & + 0.8159\left(\frac{a}{t}\right)^2\left(\frac{a}{c}\right) \end{aligned} \tag{A.17}$$

$$\begin{aligned} M_{A1}^{\frac{\pi}{4}}\left(\frac{a}{c}, \frac{a}{t}\right) = {} & 0.79844 + 0.81134\left(\frac{a}{t}\right) - 0.36419\left(\frac{a}{c}\right) - 0.35084\left(\frac{a}{t}\right)^2 + 1.2286\left(\frac{a}{c}\right)^2 - 1.0992\left(\frac{a}{t}\right)\left(\frac{a}{c}\right) - 0.5184\left(\frac{a}{t}\right)^3 - 0.6557\left(\frac{a}{c}\right)^3 + 0.1472\left(\frac{a}{t}\right)\left(\frac{a}{c}\right)^2 \\ & + 0.87011\left(\frac{a}{t}\right)^2\left(\frac{a}{c}\right) \end{aligned} \tag{A.18}$$

Expressions for reference stress intensity factors at the surface point for a stress distribution constant through the thickness:

$$K_{1r}^B = \sigma_0\sqrt{\frac{\pi a}{Q}} F_0\left(\frac{a}{c}, \frac{a}{t}\right) \cdot M_{B0}\left(\varnothing, \frac{a}{c}, \frac{a}{t}\right) \tag{A.19}$$

where

$$F_0\left(\frac{a}{c}, \frac{a}{t}\right) = \left[C_0 + C_1\left(\frac{a}{t}\right)^2 + C_2\left(\frac{a}{t}\right)^4\right]\sqrt{\frac{a}{c}} \tag{A.20}$$

$$C_0 = 1.2972 - 0.1548\left(\frac{a}{c}\right) - 0.0185\left(\frac{a}{c}\right)^2 \tag{A.21}$$

$$C_1 = 1.5083 - 1.3219\left(\frac{a}{c}\right) + 0.5128\left(\frac{a}{c}\right)^2 \tag{A.22}$$

$$C_2 = -1.101 - \frac{0.879}{0.157 + \left(\frac{a}{c}\right)} \tag{A.23}$$

and

$$M_{B0}\left(\varnothing, \frac{a}{c}, \frac{a}{t}\right) = \frac{(\varnothing - 45)(\varnothing - 30)}{1350} - \frac{\varnothing(\varnothing - 45)}{450} M_{B0}^{\frac{\pi}{6}}\left(\frac{a}{c}, \frac{a}{t}\right) + \frac{\varnothing(\varnothing - 30)}{675} M_{B0}^{\frac{\pi}{4}}\left(\frac{a}{c}, \frac{a}{t}\right) \tag{A.24}$$

$$\begin{aligned} M_{B0}^{\frac{\pi}{6}}\left(\frac{a}{c}, \frac{a}{t}\right) = {} & 0.8689 + 0.2130\left(\frac{a}{t}\right) + 0.0596\ln\left(\frac{a}{c}\right) - 0.6162\left(\frac{a}{t}\right)^2 + 0.0931\left[\ln\left(\frac{a}{c}\right)\right]^2 - 0.2956\left(\frac{a}{t}\right)ln\left(\frac{a}{c}\right) + 0.9321\left(\frac{a}{t}\right)^3 + 0.005162\left[\ln\left(\frac{a}{c}\right)\right]^3 \\ & - 0.1592\left(\frac{a}{t}\right)\left[\ln\left(\frac{a}{c}\right)\right]^2 - 0.06520\left(\frac{a}{t}\right)^2 ln\left(\frac{a}{c}\right) \end{aligned} \tag{A.25}$$

$$\begin{aligned} M_{B0}^{\frac{\pi}{4}}\left(\frac{a}{c}, \frac{a}{t}\right) = {} & 0.8615 + 0.2410\left(\frac{a}{t}\right) + 0.1587\ln\left(\frac{a}{c}\right) - 0.64955\left(\frac{a}{t}\right)^2 + 0.1775\left[\ln\left(\frac{a}{c}\right)\right]^2 - 0.3313\left(\frac{a}{t}\right)ln\left(\frac{a}{c}\right) + 0.7929\left(\frac{a}{t}\right)^3 + 0.01811\left[\ln\left(\frac{a}{c}\right)\right]^3 \\ & - 0.2125\left(\frac{a}{t}\right)\left[\ln\left(\frac{a}{c}\right)\right]^2 - 0.3553\left(\frac{a}{t}\right)^2\ln\left(\frac{a}{c}\right) \end{aligned} \tag{A.26}$$

Expressions for reference stress intensity factors at the surface point for a stress distribution linearly decreasing through the thickness:

$$K_{2r}^B = \sigma_0\sqrt{\frac{\pi a}{Q}} F_1\left(\frac{a}{c}, \frac{a}{t}\right) M_{B1}\left(\varnothing, \frac{a}{c}, \frac{a}{t}\right) \tag{A.27}$$

where

$$F_1\left(\frac{a}{c}, \frac{a}{t}\right) = \left[D_0 + D_1\left(\frac{a}{t}\right)^2 + D_2\left(\frac{a}{t}\right)^4\right]\sqrt{\frac{a}{c}} \tag{A.28}$$

$$D_0 = 1.2687 - 1.0642\left(\frac{a}{c}\right) + 1.4646\left(\frac{a}{c}\right)^2 - 0.7250\left(\frac{a}{c}\right)^3 \tag{A.29}$$

$$D_1 = 1.1207 - 1.2289\left(\frac{a}{c}\right) + 0.5876\left(\frac{a}{c}\right)^2 \tag{A.30}$$

$$D_2 = 0.190 - 0.608\left(\frac{a}{c}\right) + \frac{0.199}{0.035 + \left(\frac{a}{c}\right)} \tag{A.31}$$

and

$$M_{B1}\left(\varnothing, \frac{a}{c}, \frac{a}{t}\right) = \frac{(\varnothing - 45)(\varnothing - 30)}{1350} - \frac{\varnothing(\varnothing - 45)}{450} M_{B1}^{\frac{\pi}{6}}\left(\frac{a}{c}, \frac{a}{t}\right) + \frac{\varnothing(\varnothing - 30)}{675} M_{B1}^{\frac{\pi}{4}}\left(\frac{a}{c}, \frac{a}{t}\right) \tag{A.32}$$

$$\begin{aligned} M_{B1}^{\frac{\pi}{6}}\left(\frac{a}{c}, \frac{a}{t}\right) = {} & 0.8483 + 0.1317\left(\frac{a}{t}\right) + 0.03697\ln\left(\frac{a}{c}\right) - 0.387\left(\frac{a}{t}\right)^2 + 0.08202\left[\ln\left(\frac{a}{c}\right)\right]^2 - 0.2261\left(\frac{a}{t}\right)\ln\left(\frac{a}{c}\right) + 0.7143\left(\frac{a}{t}\right)^3 + 0.002463\left[\ln\left(\frac{a}{c}\right)\right]^3 \\ & - 0.1209\left(\frac{a}{t}\right)\left[\ln\left(\frac{a}{c}\right)\right]^2 - 0.07085\left(\frac{a}{t}\right)^2\ln\left(\frac{a}{c}\right) \end{aligned} \tag{A.33}$$

$$\begin{aligned} M_{B1}^{\frac{\pi}{4}}\left(\frac{a}{c}, \frac{a}{t}\right) = {} & 0.8344 + 0.09865\left(\frac{a}{t}\right) + 0.07959\ln\left(\frac{a}{c}\right) - 0.023849\left(\frac{a}{t}\right)^2 + 0.10558\left[\ln\left(\frac{a}{c}\right)\right]^2 - 0.2268\left(\frac{a}{t}\right)\ln\left(\frac{a}{c}\right) + 0.11467\left(\frac{a}{t}\right)^3 + 0.00211\left[\ln\left(\frac{a}{c}\right)\right]^3 \\ & - 0.1562\left(\frac{a}{t}\right)\left[\ln\left(\frac{a}{c}\right)\right]^2 - 0.29802\left(\frac{a}{t}\right)^2\ln\left(\frac{a}{c}\right) \end{aligned} \tag{A.34}$$

## References


[1] G. Labeas, I. Diamantakos, Laser beam welding residual stresses of cracked T-joints, Theor. Appl. Fract. Mech. 63–64 (2013) 69–76.
[2] M. Moattari, M.M. Shokrieh, H. Moshayedi, Effects of residual stresses induced by repair welding on the fracture toughness of Ni-based IN939 alloy, Theor. Appl. Fract. Mech. 108 (2020), 102614.
[3] T. Kitada, H. Nakai, T. Furuta, A study on initial deflections and residual stresses in steel plates with closed cross-sectional stiffeners, Doboku Gakkai Ronbunshu. 428 (1991) 127–136 [in Japanese].
[4] Q. Zhao, Z. Guo, X. Shen, B. Briseghella, Test study on residual stress distribution of hybrid steel u-rib stiffened plates, J Constr Steel Res. 121 (2016) 261–267.
[5] E.V. Puymbroeck, G.V. Staen, N. Iqbal, H.D. Backer, Residual weld stresses in stiffener-to-deck plate weld of an orthotropic steel deck, J Constr Steel Res. 159 (2019) 534–547.
[6] B. Qiang, Y.D. Li, C.R. Yao, X. Wang, Through-thickness welding residual stress and its effect on stress intensity factors for semi-elliptical surface cracks in a butt-welded steel plate, Eng. Fract. Mech. 193 (2018) 17–31.
[7] B. Qiang, Y.D. Li, C.R. Yao, X. Wang, Y. Gu, Through-thickness distribution of residual stresses in Q345qD butt-welded steel plates, Journal of Materials Processing Tech. 251 (2018) 54–64.
[8] A. Jacob, J. Oliveira, A. Mehmanparast, F. Hosseinzadeh, J. Kelleher, F. Berto, Residual stress measurements in offshore wind monopile weldments using neutron diffraction technique and contour method, Theor. Appl. Fract. Mech. 96 (2018) 418–427.
[9] R. Gadallah, S. Tsutsumi, T. Yonezawa, H. Shimanuki, Residual stress measurement at the weld root of rib-to-deck welded joints in orthotropic steel bridge decks using the contour method, Eng. Struct. 219 (2020), 110946.
[10] K.W. Jones, M.L. Dunn, Fatigue crack growth through a residual stress field introduced by plastic beam bending, Fatigue Fract. Eng. Mater. Struct. 31 (2008) 863–875.
[11] Z.G. Xiao, K. Yamada, S. Ya, X.L. Zhao, Stress analyses and fatigue evaluation of rib-to-deck joints in steel orthotropic decks, Int. J. Fatigue 30 (2008) 1387–1397.
[12] H.T. Nguyen, Q.T. Chu, S.E. Kim, Fatigue analysis of a pre-fabricated orthotropic steel deck for light-weight vehicles, J. Constr. Steel Res. 67 (2011) 647–655.
[13] R. Liu, Y. Liu, B. Ji, M. Wang, Y. Tian, Hot spot stress analysis on rib–deck welded joint in orthotropic steel decks, J. Constr. Steel Res. 97 (2014) 1–9.
[14] M. Yang, B. Ji, Z. YuanZhou, Z. Fu, Fatigue behavior and strength evaluation of vertical stiffener welded joint in orthotropic steel decks, Eng. Fail. Anal. 70 (2016) 222–236.
[15] ABAQUS. Inc., Version. 6 (2010) 10.
[16] Z. YuanZhou, B. Ji, Z. Fu, et al., Local stress variation in welded joints by ICR treatment, J Constr Steel Res 120 (2016) 45–51.
[17] D. Deng, H. Murakawa, Numerical simulation of temperature field and residual stress in multi-pass welds in stainless steel pipe and comparison with experimental measurements, Comput Mater Sci. 37 (2003) 269–277.
[18] D. Deng, H. Murakawa, Prediction of welding distortion and residual stress in a thin plate butt-welded joint, Comput Mater Sci. 43 (2008) 353–365.
[19] ESI Group. SYSWELD Ver; 2012.
[20] ASTM E837-13a. Standard test method for determining residual stresses by hole-drilling strain-gage method. ASTM International; 2013.
[21] B. Qiang, Y.D. Li, Y. Gu, D. Boko-haya, Uncertainty of strain release coefficients for the blind-hole procedure evaluated by Monte Carlo simulation, Mater. Test. 59 (2017) 630–634.
[22] GB/T 31310–2014.Metallic material-determination of residual stress-Hole drilling strain-gauge method. Beijing: Standards Press of China; 2014. [in Chinese].
[23] J. Goldak, A. Chakravarti, M. Bibby, A new finite element model for welding heat sources, Metallurgical and Materials Transactions B 15 (2) (1984) 299–305.
[24] D. Deng, S. Kiyoshima, Numerical simulation of welding temperature field, residual stress and deformation induced by electro slag welding, Comput. Mater. Sci. 62 (2012) 23–34.
[25] J.A. Francis, M. Turski, P.J. Withers, Measured residual stress distributions for low and high heat input single weld beads deposited on to SA508 steel, Mater. Sci. Technol. 25 (3) (2009) 325–334.
[26] M. Rikken, R. Pijpers, H. Slot, et al., A combined experimental and numerical examination of welding residual stresses, J. Mater. Process. Technol. 261 (2018) 98–106.
[27] G. Meneghetti, P. Lazzarin, The peak stress method for fatigue strength assessment of welded joints with weld toe or weld root failures, Welding in the World 55 (7/8) (2011) 22–29.
[28] G. Meneghetti, C. Guzzella, The peak stress method to estimate the mode I notch stress intensity factor in welded joints using three-dimensional finite element models, Eng. Fract. Mech. 115 (2014) 154–171.
[29] H.F. Bueckner, A novel principle for the computation of stress intensity factors, Z Agew Math Mech 50 (1970) 129–146.
[30] J. Rice, Some remarks on elastic tip fields, Int J Solids Struct. 8 (1972) 751–758.
[31] G. Glinka, G. Shen, Universal features of weight functions for cracks in mode I, Eng. Fract. Mech. 40 (6) (1991) 1135–1146.
[32] X. Wang, S.B. Lambert, Stress intensity factors for low aspect ratio semi-elliptical surface cracks in finite thickness plates subjected to nonuniform stresses, Eng. Fract. Mech. 51 (1995) 517–532.
[33] X. Wang, S.B. Lambert, Weight functions and stress intensity factors for semi-elliptical cracks in T-plate welded joints, Fatigue Fract. Eng. Mater. Struct. 21 (1) (1998) 99–117.
[34] TB 10091-2017. Code for Design on Steel Structure of Railway Bridge. Beijing: China Railway Press, 2017 (in Chinese).
[35] Z. Qian, S. Chumbley, T. Karakulak, et al., The residual stress relaxation behavior of weldments during cyclic loading, Metallurgical and Materials Transactions A 44 (7) (2013) 3147–3156.
[36] C.H. Lee, K.H. Chang, V.N. Van Do, Finite element modeling of residual stress relaxation in steel butt welds under cyclic loading, Eng. Struct. 103 (2015) 63–71.
[37] J. Cho, C.H. Lee, FE analysis of residual stress relaxation in a girth-welded duplex stainless steel pipe under cyclic loading, Int. J. Fatigue 82 (2016) 462–473.
[38] X. Xie, W. Jiang, Y. Luo, et al., A model to predict the relaxation of weld residual stress by cyclic load: Experimental and finite element modeling, Int. J. Fatigue 95 (2017) 293–301.